BNL-108286-2015-TECH
EIC/45;BNL-108286-2015-IR

Tracking studies in eRHIC energy-recovery recirculator

F. Méot

July 2015

Collider Accelerator Department
Brookhaven National Laboratory

U.S. Department of Energy
USDOE Office of Science (SC), Basic Energy Sciences (BES)

DISCLAIMER

BNL-108286-2015-IR

eRHIC/45
July 2015

Tracking studies in eRHIC energy-recovery recirculator

**F. Meot, S. Brooks, V. Ptitsyn,
D. Trbojevic, N. Tsoupas**

**Collider-Accelerator Department
Brookhaven National Laboratory
Upton, NY 11973**

**U.S. Department of Energy
Office of Science, Office of Nuclear Physics**

Tracking studies in eRHIC energy-recovery recirculator

F. Méot, S. Brooks, V. Ptitsyn, D. Trbojevic, N. Tsoupas

BNL C-AD, Upton, LI, NY 11973

July 2015

Abstract

Beam and polarization tracking studies in eRHIC energy recovery electron recirculator are presented, based on a very preliminary design of the FFAG lattice. These simulations provide examples of some of the beam and spin optics aspects of the linear FFAG lattice concept and its application in eRHIC, they provide code benchmarking for synchrotron radiation and spin diffusion in addition, and pave the way towards end-to-end 6-D(phase-space)+3D(spin) tracking simulations.

Contents

1 Introduction

We investigated beam and spin optics in an early version of the Fixed Field Alternating Gradient (FFAG) electron recirculator of the energy recovery linac (ERL) of the eRHIC EIC [1, 2].

Two FFAG rings located along RHIC hadron ring recirculate the electron beam through a 1.322 GeV main energy recovery linac (Fig. 1). The first, low energy ring recirculates 10 beams (5 accelerated and 5 decelerated) with energies $[1.3 : 6.6 : 1.322]$ GeV. The second, high energy ring recirculates 21 beams (11 accelerated and 10 decelerated) with energies $[7.9 : 21.2 : 1.322]$ GeV. Spreader and combiner sections, 16 arms each, are placed at either end of the linac for orbit, optical, and phase matching of the 21 beams with FFAG arc lattice. The electron-hadron collisions occur in two interaction regions (the present RHIC IR6 and IR8 IPs).

The concept of linear FFAG optics was devised and developed in the late 1990s-early 2000s and found application in electron recirculator projects [1, 3]. Various cells as doublet, triplet, FODO, have been subject since then to detailed theoretical studies to derive orbit geometry, first order optical parameters, and other optimization criteria and methods [4, 5, 6, 7]. Comparisons with numerical tracking codes, including the ray-tracing code used here [8], were part of these theoretical investigations [9, 10, 11, 12].

For eRHIC lattice, a doublet cell (Fig. 2) has been retained as an optimal techno-economical compromise, based on various criteria as beam properties, synchrotron radiation (SR), and other considerations of technology and implementation in the RHIC tunnel.

In this Note various properties of the bare lattice are addressed, including dynamic acceptance, effects of synchrotron radiation, spin transport, etc. Preliminary turn-by-turn tracking results are presented, including end-to-end simulations. The ray-tracing code Zgoubi is used, as it allows tracking in FFAG lattices and includes synchrotron radiation and spin, features that have been extensively used and validated in contexts as R&D studies and machine operation over the years [13, 8].

2 eRHIC FFAG lattice

The present study is limited in its scope and outcomes, in particular the high energy ring is considered since it produces the main perturbative SR effects on particle and spin dynamics. A simplified version of the ring is considered. The lattice is 6-periodic and includes a thin-lens linac in the middle of one of the 6 long straight sections, namely :

$$\text{ring} \;=\; 6 \;\times\; \left[\frac{1}{2}\text{LSS} \;-\; \text{DS} \;-\; \text{ARC} \;-\; \text{DS} \;-\; \frac{1}{2}\text{LSS}\right] \;+\; \text{linac}$$

- An arc is comprised of 138 identical BD-drift-QF-drift doublet cells with quadrupole optical axes radially shifted by 7.8 mm with respect to one another to ensure the bending (Fig. 2).

- A long straight section (LSS) is comprised of 93 such cells, however with quadrupole axes superimposed. Thus the focusing is practically identical to that in the arcs. An LSS is dispersion free, all energies share a common optical axis, aligned on quad axes.

- A dispersion suppressor (DS) is comprised of 17 of these very cells, however with quadrupole axes shift gradually changing from zero at the LSS, to 7.8 mm at the arc. Six of these DS take the 21 beams (11 up, 10 down) from their respective FFAG optical axes in the arcs onto their common axis in the downstream LSS, the other 6 DS have the reverse functionality.

The re-circulator ring has other features which are not accounted for in the present study, such as, a beam line structure aimed at steering the electron bunches to IP6 and IP8 at top energy, a spreader and a combiner section at linac ends to ensure orbit and optics matching with the arcs, as well as time of flight adjustment (TOF is energy

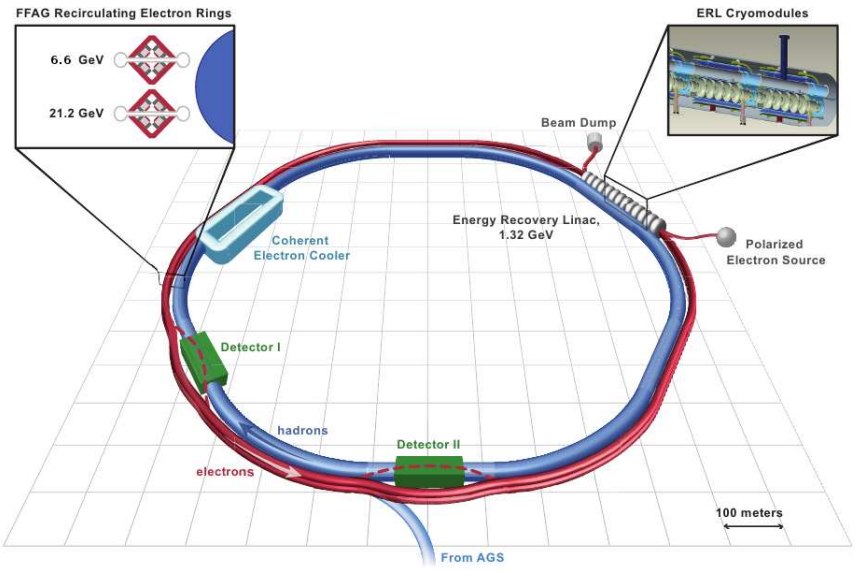

Figure 1: eRHIC rings.

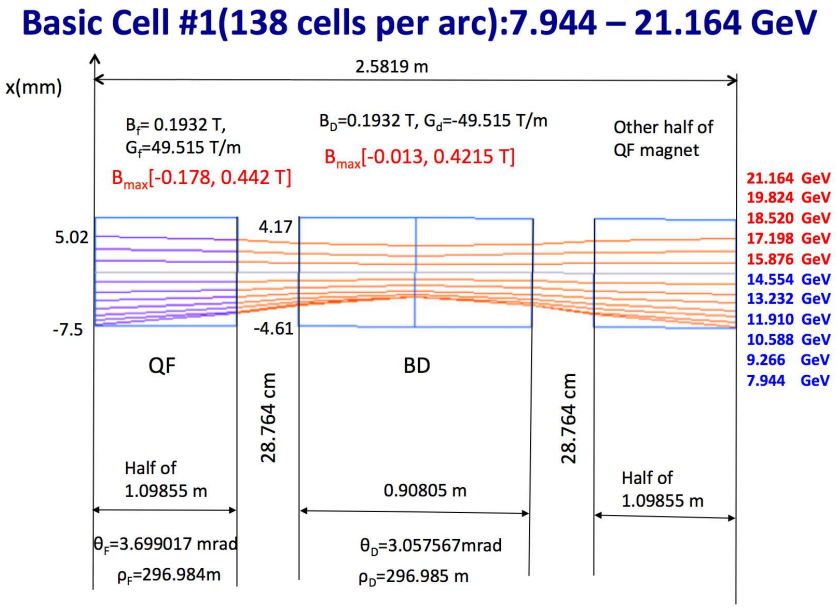

Figure 2: Arc cell in the 7.944-21.16 GeV recirculating ring. The optical axes of the QF and QD quadrupoles are displaced transversely by 7.8 mm with respect to one another.

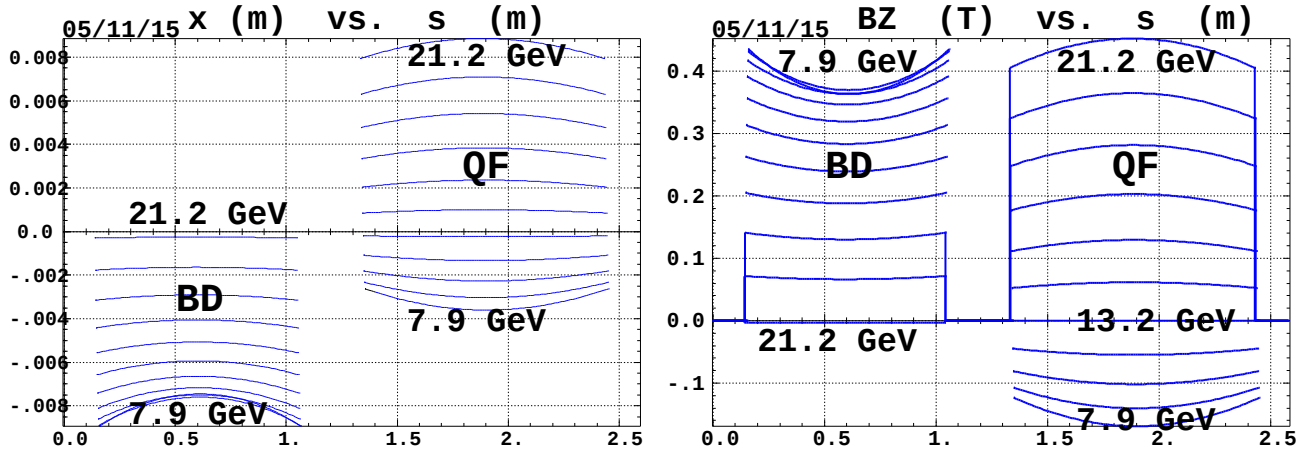

Figure 3: Left : transverse excursion of the 11 orbits across the FFAG cell, shown in the respective quadrupole frames (hence an artefact trajectory discontinuity since quadrupole axes are actually shifted transversally by 7.8 mm with respect to one another). Right : hard-edged magnetic field experienced along the 11 orbits.

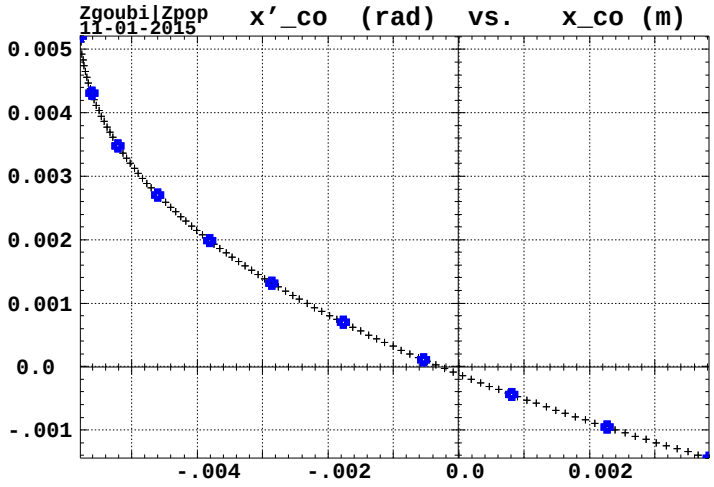

Figure 4: A scan of the FFAG orbit phase space, over the energy range 7.944 - 21.164 GeV, as observed at the center of the QF-BD drift in the arc cell. The blue markers correspond to the 11 design energies.

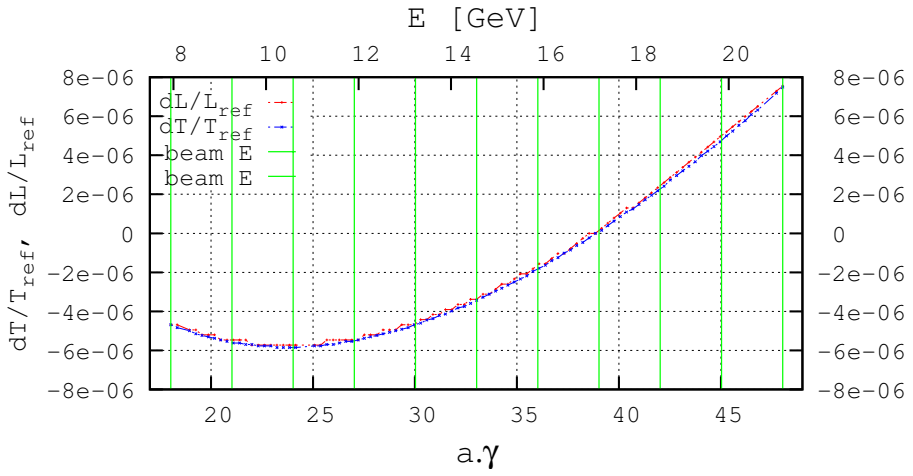

Figure 5: Parabolic (relative) variation of the cell path length and time of flight, in the 7.944 - 21.164 GeV range. The reference values are for 17.198 GeV, namely, $L_{ref} = 2.58188$ m, $T_{ref} = 8.612240$ ns. The vertical bars correspond to the 11 design energies.

dependent in the FFAG arcs). In particular, longitudinal dynamics in the simulations discussed is essentially addressed in terms of energy spread and bunch lengthening, and of their possible effect on spin dynamics. Only rough energy loss compensation is accounted for in the end-to-end tracking instances, based on the theoretical average loss (Eq. 2).

The optical properties of the 6-periodic lattice are summarized in a series of figures : Fig. 3 shows the transverse excursion and magnetic field along orbits across the arc cell, using the field modeling described in appendix A. Fig. 4 and Fig. 5 show the energy dependence of, respectively, the orbit length and time of flight. Fig. 6 shows the energy dependence of the deviation angle and curvature radius in the two quadrupoles, and the energy dependence of tunes and chromaticities. Comparisons between codes have been performed as part of these lattice studies [14], the agrrement is in general satisfying, descrepancies have been observed for some parameters though.

Note that a version of the low energy ring cell based on more realistic 3D OPERA model of the quadrupole doublet has been studied, it can be referred to for comparison [15].

Fig. 7 shows the y-precession of the horizontal spin components across the quadrupoles of the arc cell doublet, for the 11 design energies. The precession is $a\gamma\alpha$ with α the orbit deviation angle, γ the Lorentz relativistic factor and $a = 0.001159652$ the anomalous magnetic moment.

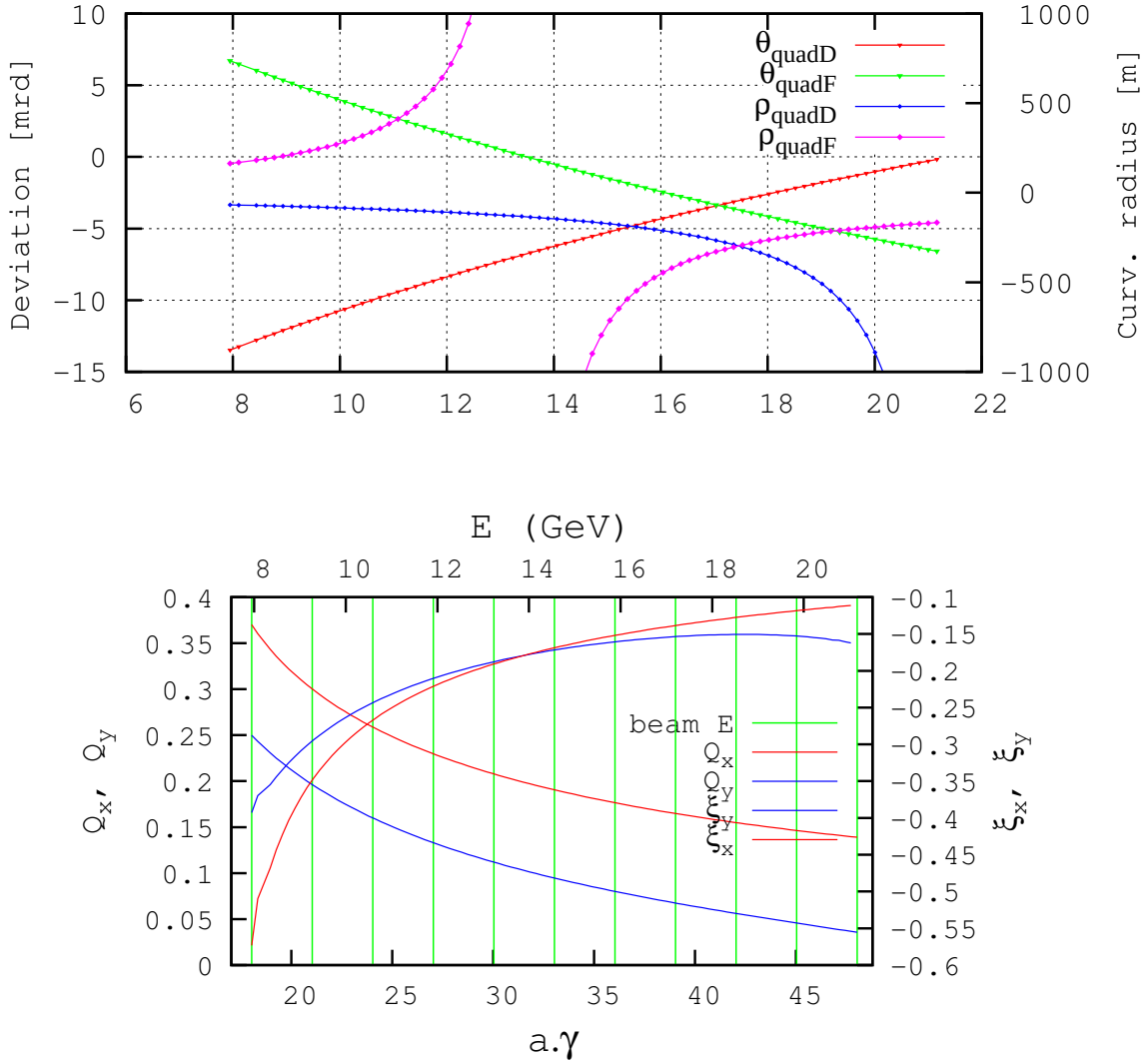

Figure 6: Top : energy dependence of orbit deviation angle and curvature radius in arc cell quadrupoles. Bottom : cell tunes and chromaticities versus energy; the vertical bars materialize the 11 design energies.

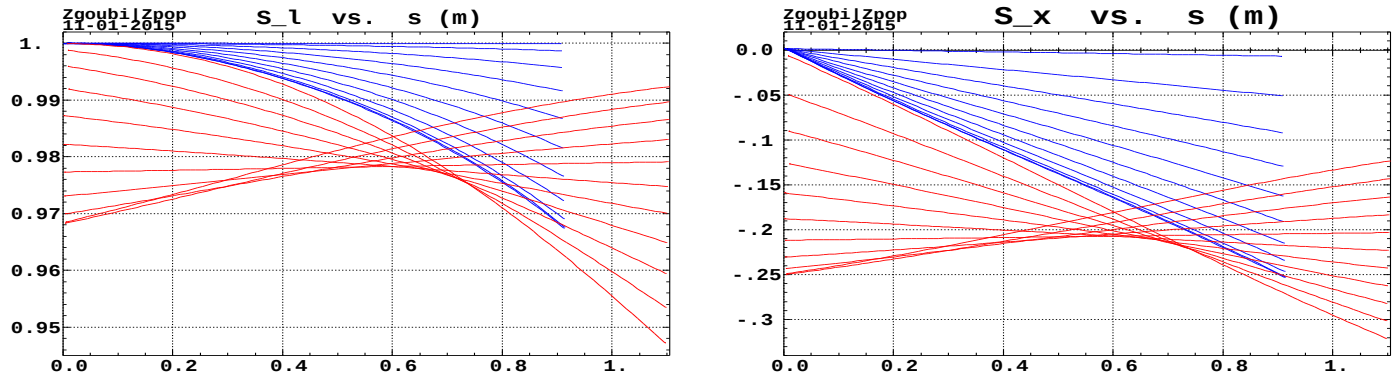

Figure 7: y-precession of the S_l (longitudinal, left) and S_x (transverse horizontal, right) on-momentum spin components along the 11 orbits across the BD (blue) and QF (red) arc cell magnets, as observed in the magnet frames, given initial longitudinal ($\vec{S} = \vec{S}_l$) spin orientation.

Orbit in the dispersion suppressors

The 12 dispersion suppressors are based on a "missing bend" scheme, where the relative displacement of the two cell quadrupoles (the origin of the dipole effect in the FFAG cell) is brought to zero over a series of cells. From orbit viewpoint, a transverse displacement $\delta x_{F,D}$ of respectively the F or D quadrupole is equivalent to a pair of identical kicks at entrance (θ_u) and exit (θ_d) of the magnet, namely [16]

$$\theta_{u,d} = K_F^{\frac{1}{2}} \tan(L_F K_F^{\frac{1}{2}}/2) \times \delta x_F$$

$$\theta_{u,d} = -|K_D|^{\frac{1}{2}} \mathrm{th}(L_D |K_D|^{\frac{1}{2}}/2) \times \delta x_D$$

with $K_{F,D}$ (resp. $L_{F,D}$) the quadrupole strength (resp. length). As a consequence the orbit builds up along the DS following

$$\frac{x_{\rm orb}(s)}{\sqrt{\beta(s)}} = \frac{x_{\rm orb}(0)}{\sqrt{\beta(0)}} \cos(\phi(s)) + \frac{\alpha(0) x_{\rm orb}(0) + \beta(0) x'_{\rm orb}(0)}{\sqrt{\beta(0)}} \sin(\phi(s)) + \sum_k \sqrt{\beta(s_k)} \theta_k \sin(\phi(s) - \phi(s_k))$$

$$\frac{\alpha(s) x_{\rm orb}(s) + \beta(s) x'_{\rm orb}(s)}{\sqrt{\beta(s)}} = -\frac{x_{\rm orb}(0)}{\sqrt{\beta(0)}} \sin(\phi(s)) + \frac{\alpha(0) x_{\rm orb}(0) + \beta(0) x'_{\rm orb}(0)}{\sqrt{\beta(0)}} \cos(\phi(s)) + \sum_k \sqrt{\beta(s_k)} \theta_k \cos(\phi(s) - \phi(s_k))$$

with $\theta_k = \theta_u$ or θ_d, and either (i) $x_{\rm orb}(0)$ and $x'_{\rm orb}(0)$ the FFAG orbit coordinates in the arc→LSS case, or (ii) $x_{\rm orb}(0) = 0$, $x'_{\rm orb}(0) = 0$ in the LSS→arc case. Fig. 8 shows the orbit build-up from LSS to arc, ending up at the arc with (x,x') coordinates which do not coincide with the periodic orbit of the arc FFAG cell. The orbit build-up depends on the phase advance $\phi(s) = \int_0^s \frac{ds}{\beta(s)}$. Thus it depends on the cell tune, and on energy. Fig. 9 shows the resulting orbit build-up in the arcs over 6 consecutive arcs at 5 different energies, 7.9, 9.3, 10.6, 11.9GeV and 13.2 GeV. In each case the starting coordinates (at $s = 0$ in the figure, *i.e.*, downstream end of the LSS) are taken $(x, x') = (0, 0)$. Fig. 10 illustrates the tune dependence of the orbit amplification in the case of pass #4 (11.9 GeV) - for simplicity energy is changed instead of tunes, with the correlation given in Fig. 6. The orbit excursion is reduced to below 0.1 mm for $E = 11.9$ GeV$+1\%$.

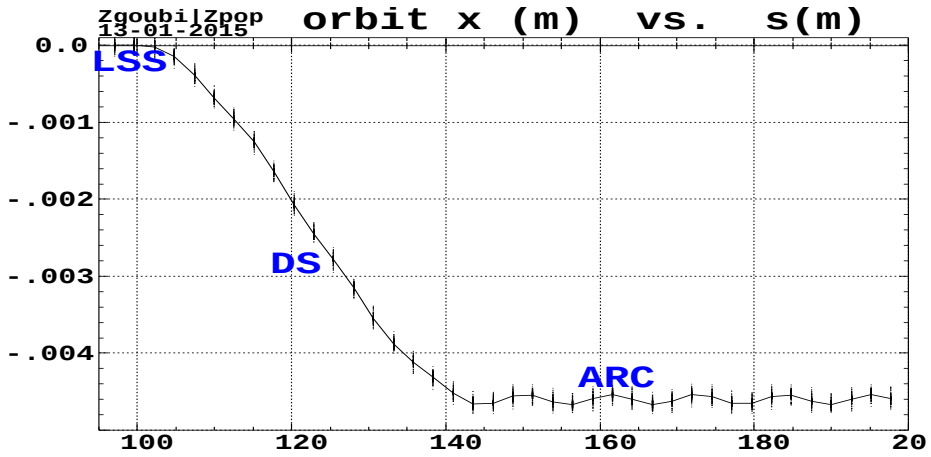

Figure 8: Case of the 11.9GeV pass. The orbit is shown from downstream end of LSS to upstream region of following arc.

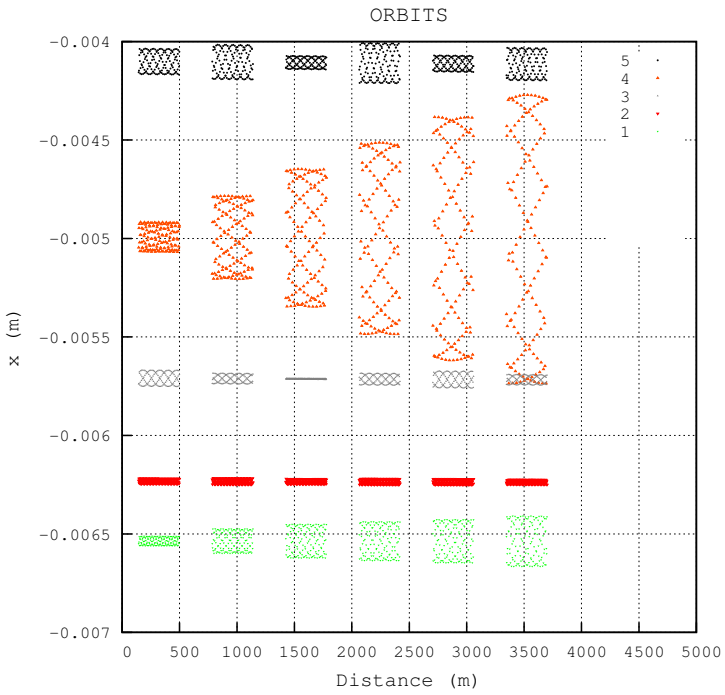

Figure 9: Orbit build-up over a single pass, for 7.9, 9.3, 10.6, 11.9GeV and 13.2 GeV (bottom to top). In each case, the orbit leaves the LSS with zero coordinates, it is then recorded along the 6 consecutive arcs.

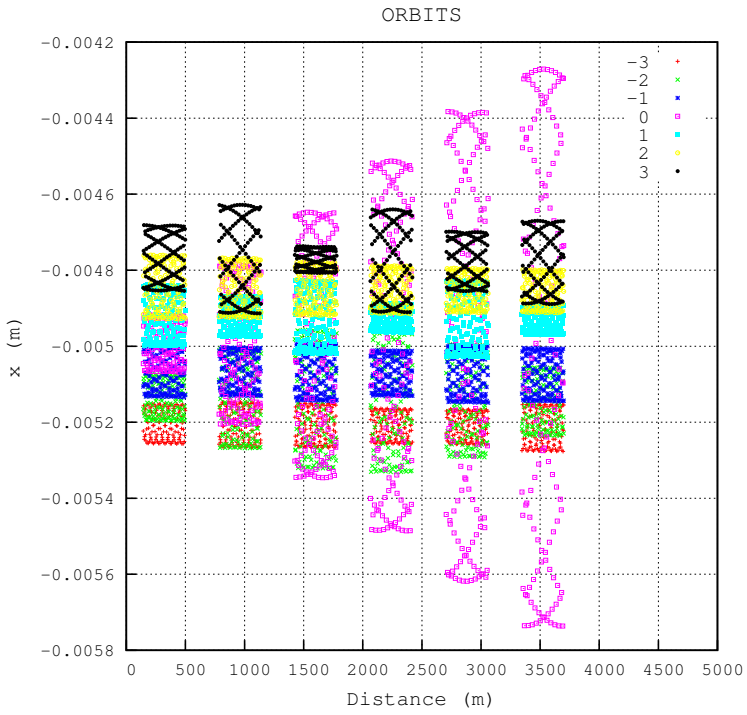

Figure 10: The orbit is computed for 7 different energies $E + dE$ in the vicinity of $E = 11.9$ GeV, namely for $dE/E = 0, \pm 1, \pm 2, \pm 3\%$. The total orbit excursion as observed in the arcs is down to 0.08 mm is for $dE/E = 1\%$.

3 Synchrotron radiation

The SR induced energy loss relative to the the bunch centroid and the energy spread write, respectively

$$\frac{\overline{\Delta E}}{E_{\rm ref}} = 1.9 \times 10^{-15} \frac{\gamma^3 \Delta\theta}{\rho}, \frac{\sigma_E}{E_{\rm ref}} = 3.8 \times 10^{-14} \frac{\gamma^{\frac{5}{2}} \sqrt{\Delta\theta}}{\rho} \tag{1}$$

with $\Delta\theta$ the arc length and $1/\rho$ the curvature, assumed constant over $\Delta\theta$. Taking for average radius, in QF (focusing quad) and BD (defocusing quad) respectively, $\rho_{\rm BD} \approx \frac{s_{\rm BD}}{\Delta\theta_{\rm BD}}$, $\rho_{\rm QF} \approx \frac{s_{\rm QF}}{\Delta\theta_{\rm QF}}$ (with $s_{\rm BD}$ and $s_{\rm QF}$ the arc lengths) and considering in addition, with $l_{\rm BD}$, $l_{\rm QF}$ the magnet lengths, $s_{\rm BD} \approx l_{\rm BD}$, $s_{\rm QF} \approx l_{\rm QF}$, then one gets, per cell

$$\overline{\Delta E}[MeV] \approx 0.96 \times 10^{-15} \gamma^4 \left(\frac{l_{\rm BD}}{\rho_{\rm BD}^2} + \frac{l_{\rm QF}}{\rho_{\rm QF}^2} \right) \tag{2}$$

Taking in addition $< (1/\rho)^2 > \approx 1/ < \rho^2 >$, an estimate of the energy spread is

$$\sigma_E \approx 1.94 \times 10^{-14} \gamma^{7/2} \sqrt{\frac{l_{\rm BD}}{|\rho_{\rm BD}^3|} + \frac{l_{\rm QF}}{|\rho_{\rm QF}^3|}} \tag{3}$$

This is illustrated for a 6-arc ring (no LSS and no DS sections) in Fig. 11, where it is also compared with Monte Carlo tracking, the agreement is at % level [1]. The energy loss shows a local minimum in the $a\gamma = 30 - 35$ region, a different behavior from the classical γ^4 dependence in an isomagnetic lattice, due to the large variation of the curvature radius over the 7.9→21.2 GeV energy range (Fig. 6).

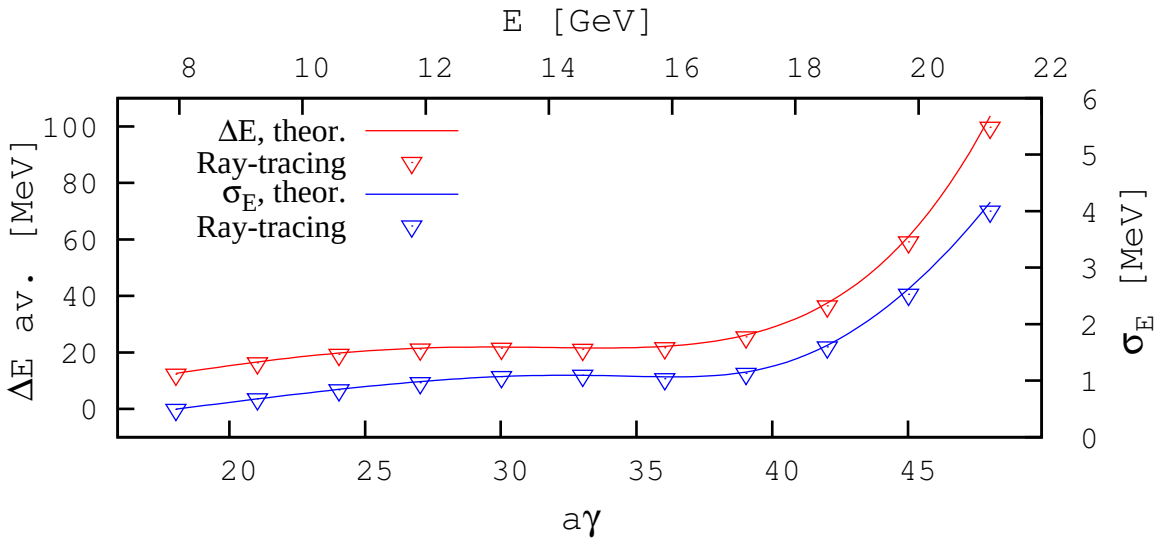

Figure 11: Average energy loss (left axis) and energy spread (right axis). Solid lines : theory (Eqs. 2 and 3) for a 6-arc ring. Markers : tracking with Monte Carlo SR (see sample tracking outcomes in Fig. 12).

The bunch lengthening over a $[s, s_f]$ distance, resulting from the stochastic energy loss, can be written [20],

$$\sigma_l = \left(\frac{\sigma_E}{E}\right) \left[\frac{1}{L_{\rm bend}} \int_s^{s_f} \left(D_x(s) T_{51}(s_f \leftarrow s) + D'_x(s) T_{52}(s_f \leftarrow s) - T_{56} \right)^2 ds \right]^{1/2}$$

[1] SR installation in Zgoubi dates back to the late 1990s, and has been subject to extensive benchmarking, including damping in rings and coupling [17].

with the integral being taken over the bends, D_x and D'_x the dispersion function and its derivative, T_{5i} the trajectory lengthening coefficient of the first order mapping ($i = 1, 2, 5, 6$ stand for respectively x, x', δl, $\delta p/p$ coordinates).

The energy loss causes a drift of the bunch centroid, as well as an horizontal emittance increase, both can be computed from the lattice parameters in the linear approximation [20, 21, 22]. Fig. 13 illustrates these effects over a 21.164 GeV recirculation (with bunch re-centering on the reference optical axis at each of the six LSS).

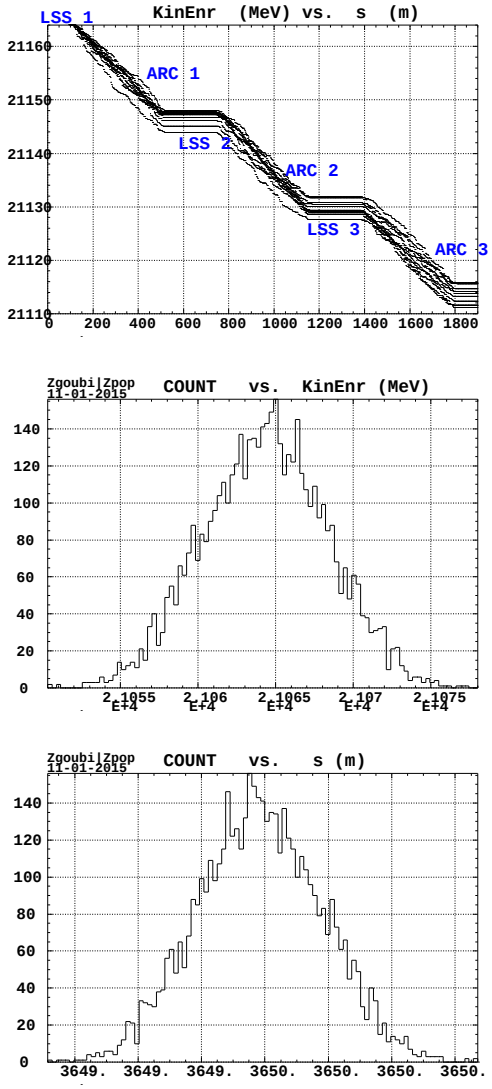

Figure 12: Top : stochastic energy decrease of a few particles over the first 3 arcs at $E_{\rm ref} = 21.164$ GeV. Middle : final energy spread in a 5000 particle bunch after the 21.164 GeV pass, $\frac{\sigma_E}{E} = 1.9 \times 10^{-4}$ around $\frac{\overline{\Delta E}}{E} = -4.7 \times 10^{-3}$ average energy loss. Bottom : longitudinal bunch distribution.

Cumulative effect of SR, over a complete 7.94→21.2→7.94 GeV cycle, is illustrated in Fig. 14 : (i) energy spread, $\sigma_E/E = 2.6 \times 10^{-4}$ at 21.1 GeV and $\sigma_E/E = 8.4 \times 10^{-4}$ back at 7.944 GeV ; (ii) bunch lengthening, $\sigma_l = 2$ mm at 21.1 GeV and $\sigma_l = 2.5$ mm back down to 7.944 GeV ; (iii) normalized horizontal emittance (from zero starting value), namely, $\epsilon_x = 20$ μm at 21.1 GeV (with strong contribution from uncompensated chromatic effects), and $\epsilon_x = 8$ μm back at 7.944 GeV.

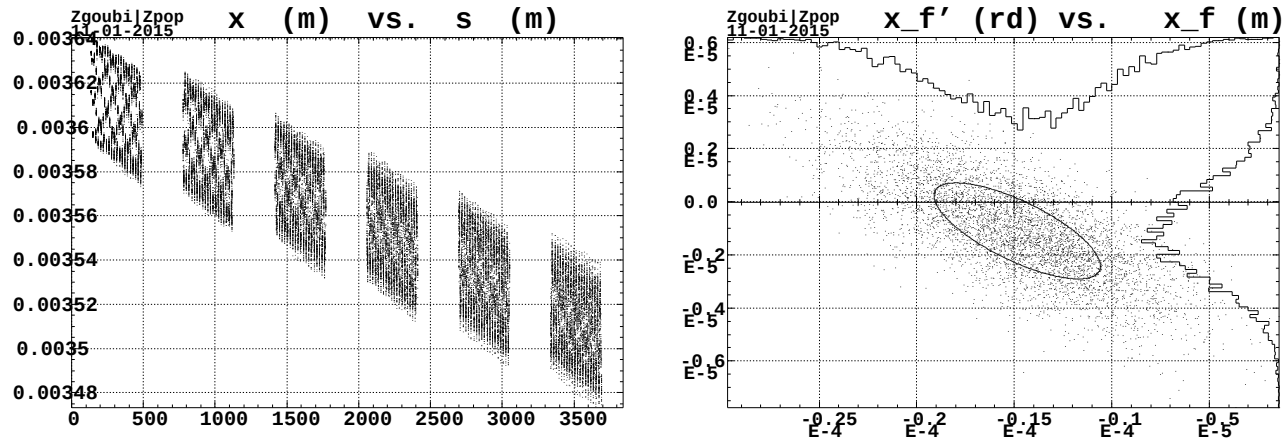

Figure 13: Left : SR loss induced x-drift along the 6 arcs of eRHIC ring, at $E = 21.164$ GeV (shown are a few particles in a bunch launched on the LSS axis with zero initial 6-D emittance). Right : a 5000 particle bunch, horizontal phase space after that complete turn, featuring $\overline{x_f} = -15$ μm, $\sigma_{x_f} = 4.3$ μm, $\overline{x'_f} = -1.1.$ μrad, $\sigma_{x'_f} = 1.8$ μrad.

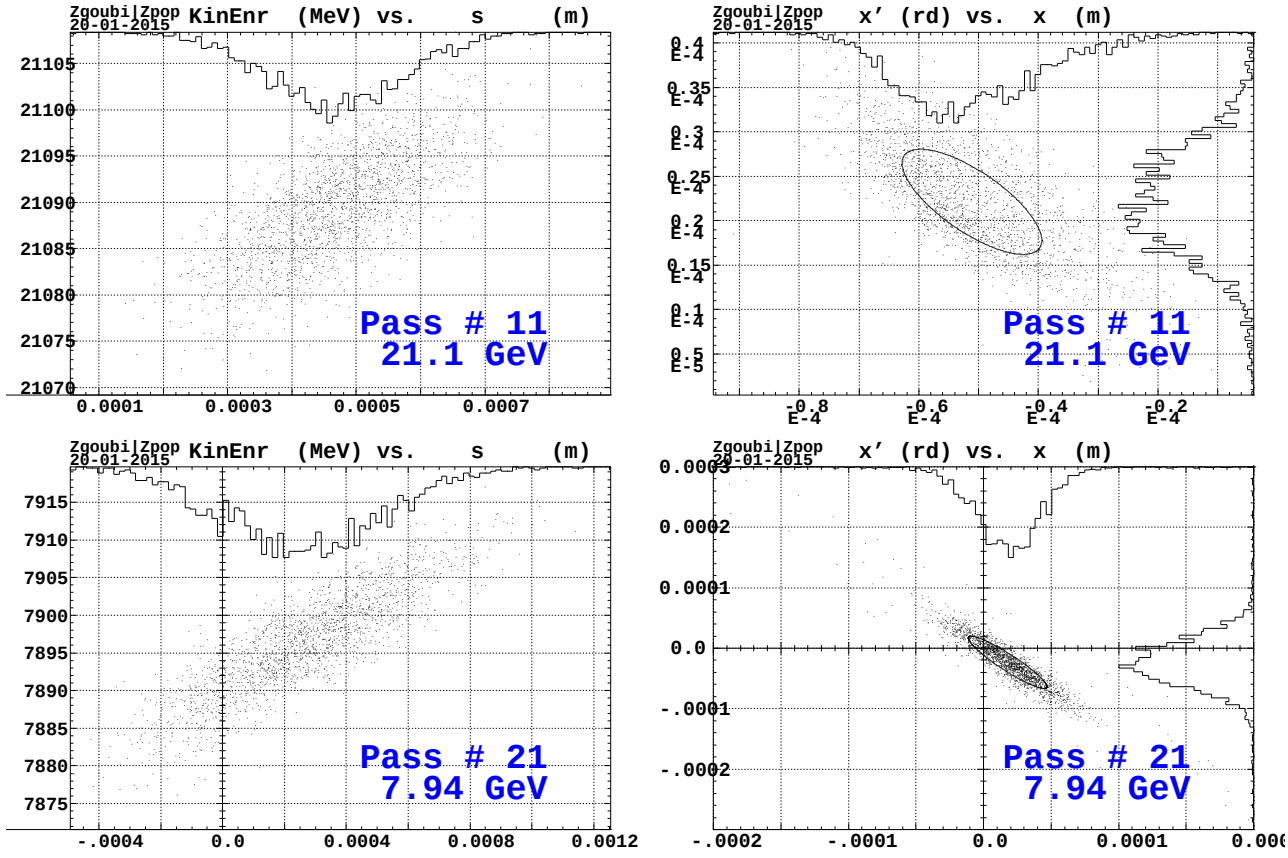

Figure 14: Cumulated effects of SR (initial 6D emittance zero), in longitudinal (left column) and radial (right column) phase space, over 21 passes in eRHIC (from 7.944 GeV to 21.164 GeV, and back down to 7.944 GeV). Top row : at collision energy, end of pass #11. Bottom row : back to injection energy after 21 re-circulations.

3.1 Dynamical acceptance

SR is off in these DA computations, SR causes emittance growth thus reducing the space available for the beam at injection into a recirculation.

3.2 Arc cell

Fig. 15 shows the 1000-cell (which is about the total number of cells in the 6 arcs that make up eRHIC ring) dynamic acceptance, in the case of, respectively, a hard-edge model and a soft fall-off model. The field model in the former case is that of Fig. 3. The field model in the latter case is shown in appendix B (Fig. 29, page 22).

3.3 Full ring

The complete ring

$$6 \times \left[\frac{1}{2}\mathrm{LSS} - \mathrm{DS} - \mathrm{ARC} - \mathrm{DS} - \frac{1}{2}\mathrm{LSS}\right]$$

is considered here.

The naturally large dynamical acceptance of the linear lattice shrinks with magnet misalignment and field defects, this is illustrated in Fig. 16.

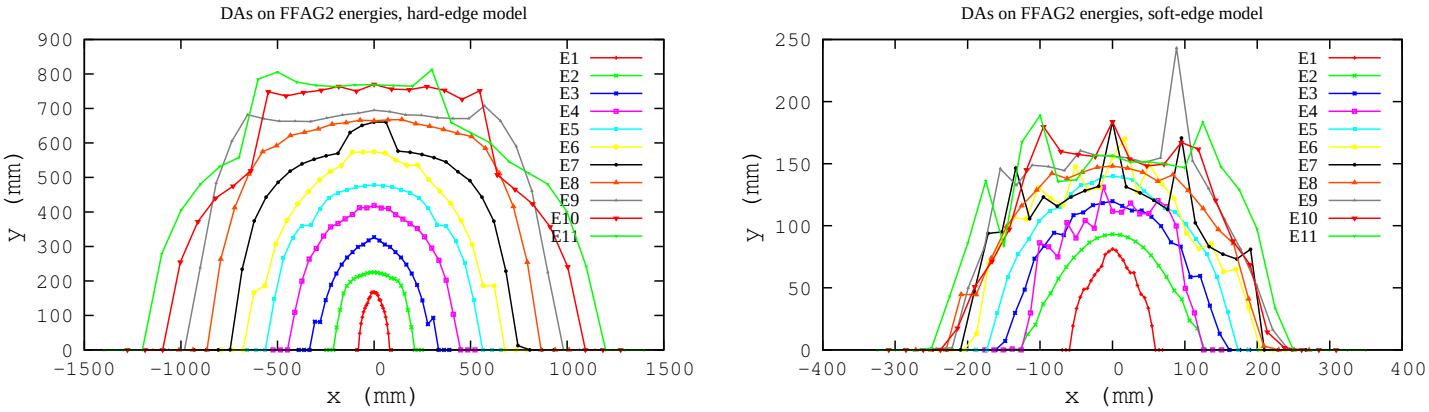

Figure 15: 1000-pass DA of the arc cell. Left : hard-edge field model, right : soft-edge model.

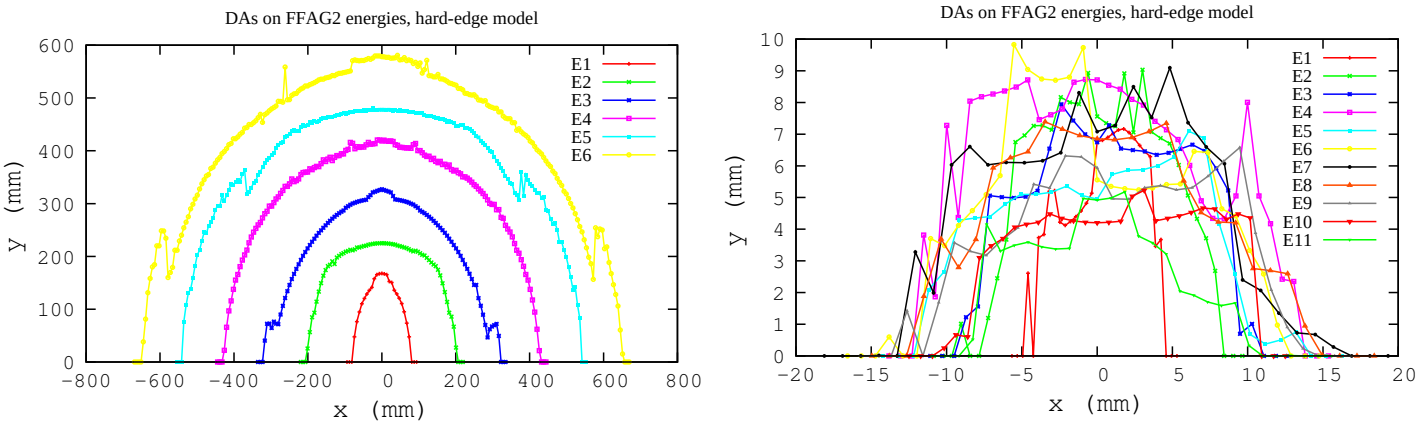

Figure 16: Available injection window into the ring at mid-LSS, for each of the 11 beams, observed at the center of an LSS. Left : defect-free lattice. Right : in the presence of a dodecapole defect in all quads of the ring, ± 3 Gauss at 1 cm, random uniform.

3.4 Multipole defects

Fig. 17 illustrates a different way of looking at tolerances, *e.g.* here in the presence of a dodecapole defect in all quadrupoles of the ring (*i.e.*, same working hypotheses as for Fig. 16-right). Defect values from 0.01 G to 30 G at 1 cm radius have been investigated (the field gradient is 50 T/m, hence a relative defect in a range $2 \times 10^{-6} - 6 \times 10^{-3}$). A 5000-particle bunch is launched with $\epsilon_x \approx \epsilon_y \approx 50\,\pi\mu$m and 10^{-4} *rms* energy spread, for 21 circulations in a complete ring ($6 \times \left[\frac{1}{2}\text{LSS} - \text{DS} - \text{ARC} - \text{DS} - \frac{1}{2}\text{LSS}\right]$ + Linac).

SR loss is summarily compensated at the linac, bunch position is assumed perfectly corrected at each LSS. Fig. 17 shows the evolution of the *rms* ellipse surface, pass after pass, from 7.94 to 21.16 and decelerating back to 7.94 GeV. This gives an indication of the maximum tolerable defect based on maximum tolerable emittance, *e.g.* at collision (pass 11) and/or extraction (pass 21).

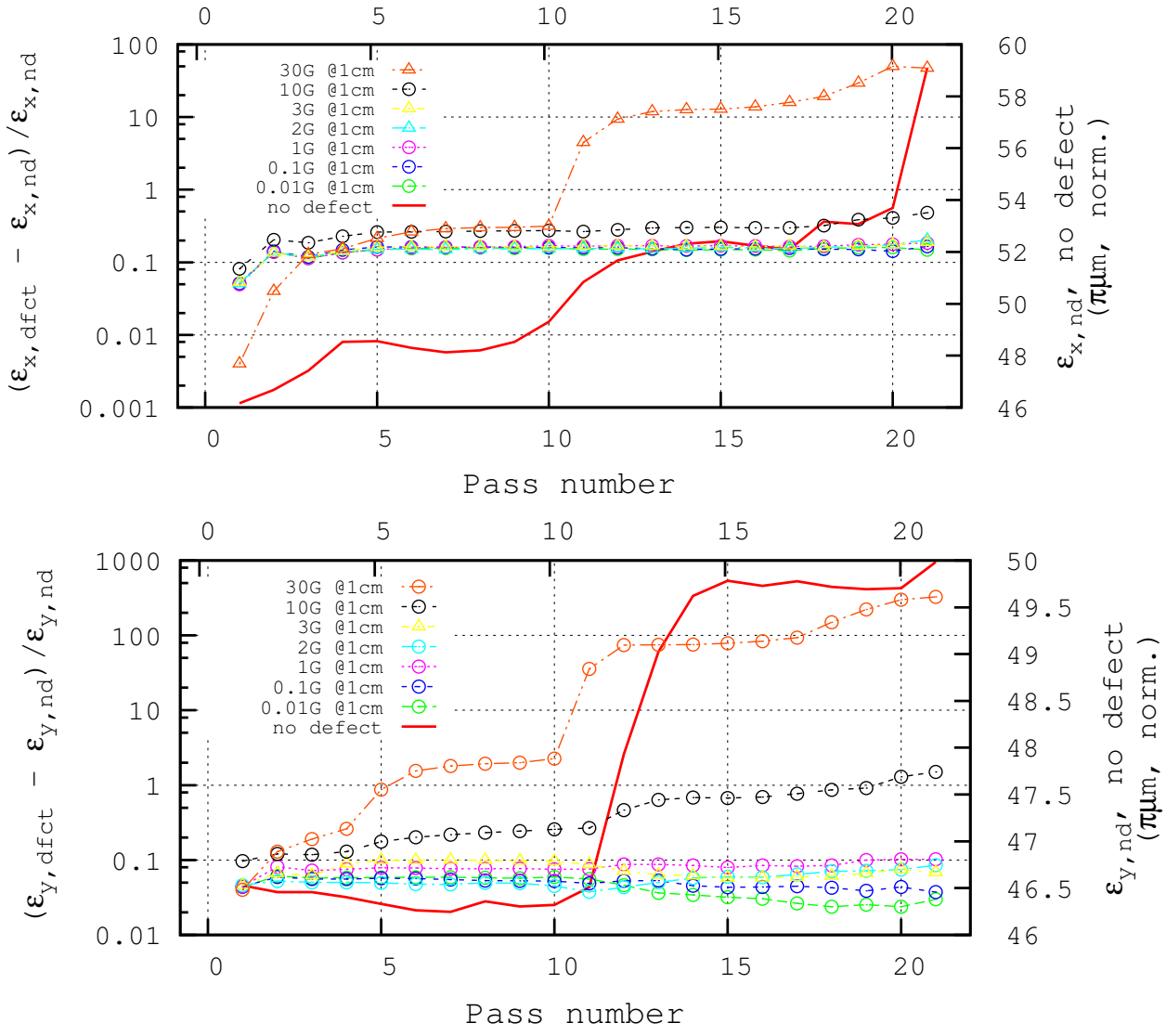

Figure 17: Evolution of the *rms* concentration ellipse surface of a re-circulated bunch, turn after turn, for various dodecapole defect strengths (from 0, to 10 Gauss at 1 cm). Left axis and markers : defect cases. Right axis and red curve : defect-free ring. Top : horizontal, bottom : vertical *rms* ellipse surface.

4 Chromatic effects

Due to the large chromaticity (Fig. 6), any beam mis-alignment results in phase extent in phase space according to $\Delta\phi = 2\pi\xi\delta E/E$.

4.1 Single turn bunch tracking, zero initial 6D emittance

SR introduces both energy spread (cf. Fig. 12) and beam shift (Fig. 13), its effect is small however compared to nominal beam emittances, it is illustrated in Fig. 18 which shows the phase-space portrait acquired by a bunch launched with zero emittances and energy spread, after a single pass in the eRHIC ring at each one of the 11 different energies, assuming orbit excursion effects in the DS regions as discussed in Sec. 2 (Figs. 8-10).

Fig. 19 compares the concentration ellipse surface ($\epsilon_x = 4\pi \times \sqrt{< x^2 >< x'^2 > - < xx' >^2}$) for the 11 different energies (note that the surface includes momentum spread contribution). The surface growth over a turn is largest when the orbit offset induced by the DS is greatest, *i.e.*, at 7.9 and 11.9 GeV, see Fig. 9. Improvement upon orbit control is confirmed in the next section (*cf.* the evolution of emittance growth from Fig. 21 (no orbit correction) to Fig. 22 (tighter orbit control)).

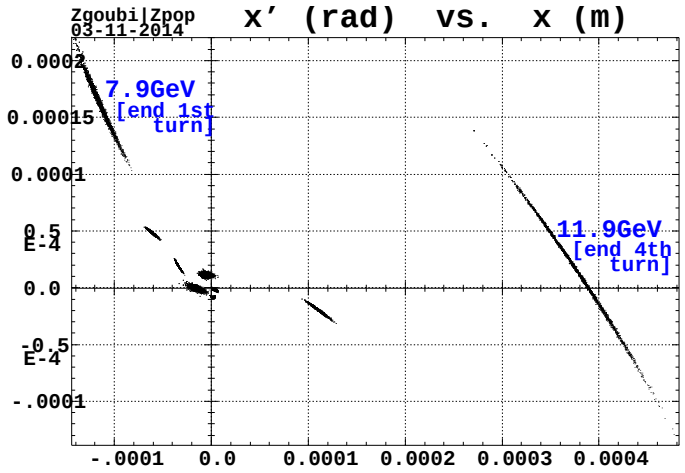

Figure 18: The 11 horizontal phase-space portraits, for 11 energies 7.944 to 21.164 GeV, step 1.322 GeV. Each phase space portrait is for a 5000 particle bunch launched on the axis of the LSS with zero starting 6D emittance. Observation point is at the center of the LSS after a full turn.

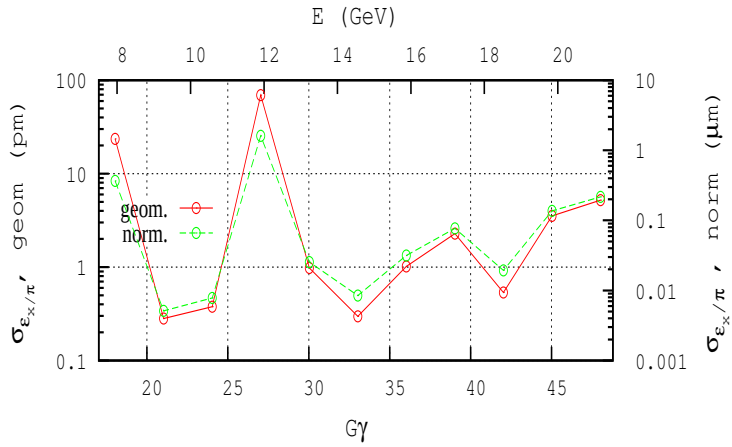

Figure 19: Comparison between the single-turn concentration ellipse surfaces, geometrical (left axis) and normalized (right axis), at the 11 design energies (the lines are to guide the eye). The surge at 7.9 GeV and at 11.9 GeV corresponds to cases of maximum orbit excursion.

4.2 Start-to-end bunch tracking, nominal initial 6D emittance

Since the chromaticity is not corrected in the eRHIC linear FFAG lattice, and given a nominal energy spread σ_E/E in the 2×10^{-4} range, thus the emittance growth is prohibitive in the absence of orbit correction. This is illustrated, for the horizontal motion, in Fig. 20 which shows the phase space portraits of a 5000-particle bunch after acceleration from 7.944 up to 21.2 GeV (collision energy), and after deceleration back to 7.944 GeV. Initial conditions at 7.944 GeV are Gaussian with *rms* $\epsilon_x \approx \epsilon_y \approx 50\,\pi\mu$m, whereas $dE/E \in [-10^{-4}, +10^{-4}]$ (random uniform).

Fig. 21 summarizes the overall *rms* concentration ellipse surface increase, over the 11 accelerated passes (from 7.944 to 21.16 GeV) followed by 10 decelerated passes (from 21.16 back to 7.944 GeV), for a bunch launched at 7.944 GeV with initial Gaussian *rms* $\epsilon_x \approx \epsilon_y \approx 50\,\pi\mu$m and $dE/E \in [-10^{-4}, +10^{-4}]$ (random uniform).

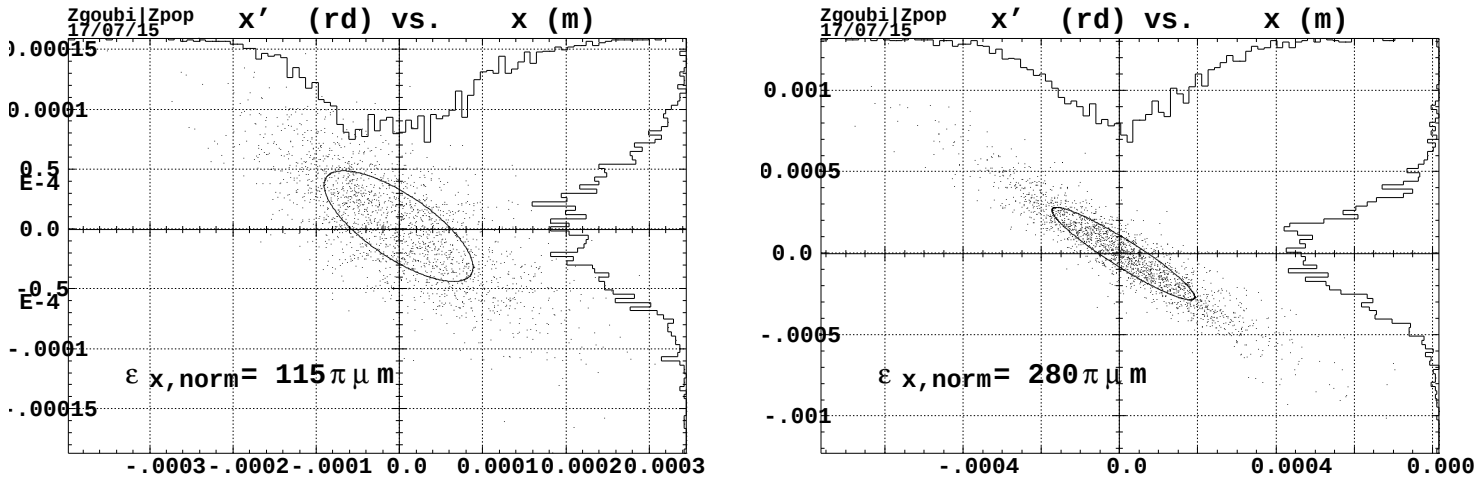

Figure 20: Horizontal phase space portrait of a bunch launched at 7.944 GeV with initial Gaussian *rms* $\epsilon_x \approx \epsilon_y \approx 50\,\pi\mu$m and $dE/E =\in [-10^{-4}, +10^{-4}]$, uniform. Left : end of the 21.2 GeV pass (collision energy), right : end of the the decelerated 7.9 GeV last pass.

In this simulation there is no vertical orbit defect whereas the bunch is (i) experiencing small misalignments in the dispersion suppressors that cause betatron oscillations in the mm range, and (ii) recentered on the theoretical reference orbit once per eRHIC turn, at the linac (*i.e.*, center of an LSS). Bunch distortion in phase space (similar to what is observed in the 7.9 GeV and 11.9 GeV cases in Fig. 18) is at the origin of the steps (local *rms* concentration ellipse surface increase) in the region $a\gamma \approx 27$ on the accelerating phase and $a\gamma \approx 38,\ 28$ on the decelerating phase.

Fig. 22 shows the much reduced emittance growth in the presence of orbit control, namely here, bunch recentering at each LSS.

Fig. 23 is obtained in the case of a vertical orbit defect caused by a small dipole error $a_0 \in [-1, +1]$Gauss, random uniform, injected in all the quadrupoles of the ring. The bunch in this case is recentered at the linac, in both transverse planes, at each turn.

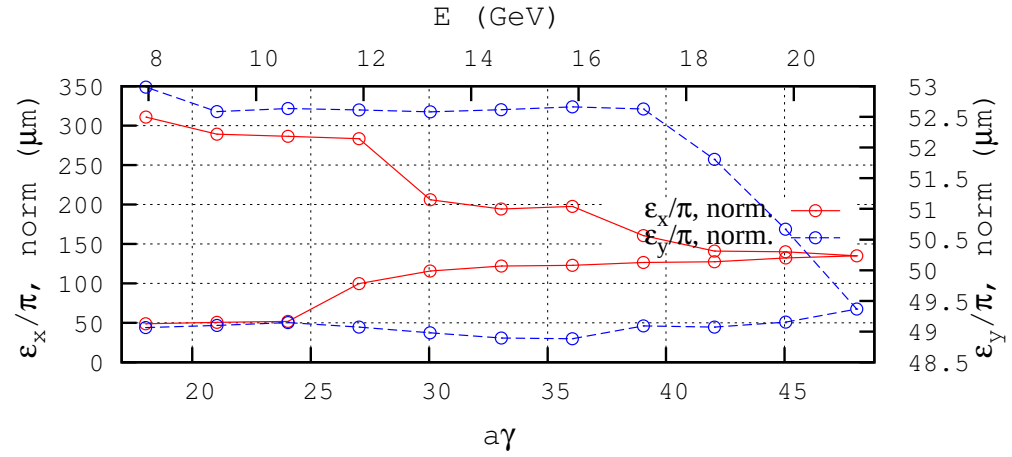

Figure 21: *rms* concentration ellipse surface after each turn. The bunch is re-centered once per turn, at the linac.

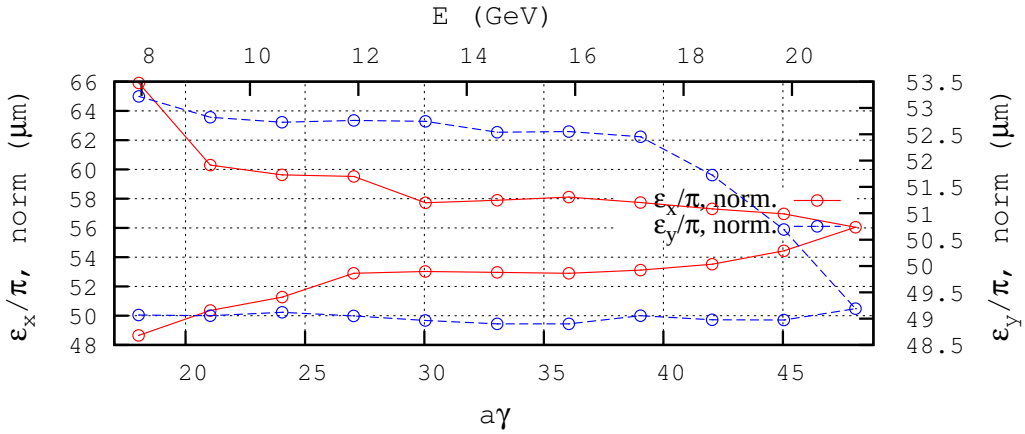

Figure 22: *rms* concentration ellipse surface after each turn. The bunch is re-centered at each of the six LSS.

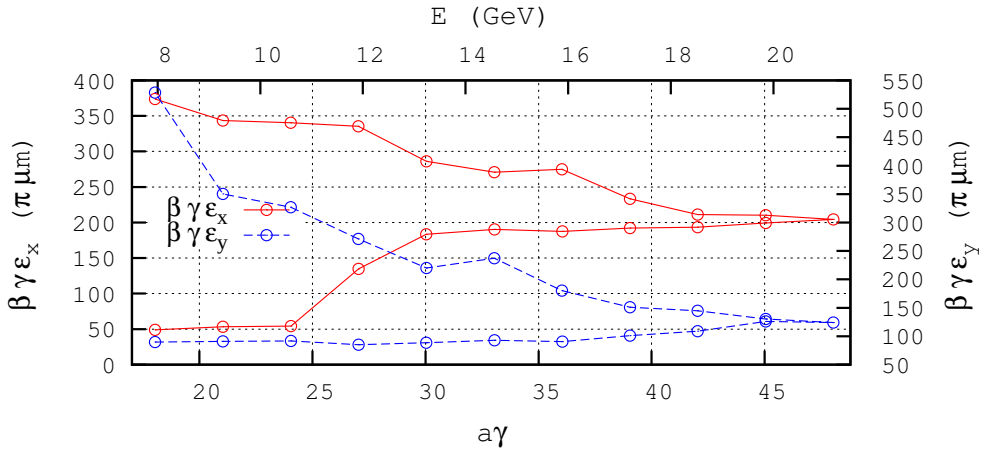

Figure 23: Evolution of the *rms* concentration ellipse surface in the presence of vertical orbit defect. Bunch recentered at linac only.

5 Polarization

Polarized electron bunch production is based on a Gatling gun [2], with a polarization of 85-90%. The electron bunch is re-circulated in eRHIC with longitudinal polarization. Spins precess at a rate $a\gamma$ per turn, with an increment of $a\Delta\gamma = 3$ at each 1.322 GeV linac boost, so ensuring the requested longitudinal spin orientation at the two IPs.

Depolarization mainly stems from energy spread (*e.g.*, a cumulated $2.5\,10^{-4}$ at 21.2 GeV from SR contribution, see Fig. 14). Spin diffusion resulting from stochastic SR also causes polarization loss, of about 2% at 21.2 GeV [2]. Non-zero vertical emittance, or vertical defects, cause spins to leave the median plane. This is illustrated in Fig. 24.

Fig. 25 monitors the evolution of the polarization (the average value of the projection, $\cos(\Delta\phi)$, of the 5000 spins on the average spin direction) and of spin angle spread σ_ϕ, in the conditions of dodecapole error simulations discussed earlier (section 3.4 and Fig. 17). Both quantities appear unchanged in this particular case, compared to the unperturbed optics (cf. σ_ϕ in Fig. 24-left).

The theoretical evolution of the spin diffusion in Fig. 24-left satisfies [28]

$$\begin{pmatrix} \overline{\Delta E^2} \\ \overline{\Delta E \Delta\phi} \\ \overline{\Delta\phi^2} \end{pmatrix} = \begin{pmatrix} 1 & 0 & 0 \\ \alpha s & 1 & 0 \\ \alpha^2 s^2 & 2\alpha s & 1 \end{pmatrix} \begin{pmatrix} \overline{\Delta E^2} \\ \overline{\Delta E \Delta\phi} \\ \overline{\Delta\phi^2} \end{pmatrix}_{s=0} + \omega \times \begin{pmatrix} s \\ \alpha s^2/2 \\ \alpha^2 s^3/3 \end{pmatrix}$$

wherein $\omega = \frac{C}{\rho^3} \lambda\!\!\!^{-}_c r_e \gamma^5 E^2 \approx 1.44 \times 10^{-27} \frac{\gamma^5}{\rho^3} E^2$ ($\lambda\!\!\!^{-}_c = \hbar/m_e c$ electron Compton wavelength, E in GeV), $C = 110\sqrt{3}/144$, $\alpha = \frac{a}{\rho E_0} \approx \frac{1}{0.4406\rho}$ (with $a = 1.16 \times 10^{-3}$, electron mass $E_0 = 0.511 \times 10^{-3}$ GeV).

Fig. 26 displays the evolution of the polarization and of the spin angle spread σ_ϕ, in the previous conditions of orbit defects : the polarization appears marginally sensible to misalignment effects of this nature and at this level. Note that the number of precessions ($a\gamma$, right vertical axis) slightly differs from an integer value, this is essentially an indication of a residual effect in the present rough compensation of SR energy loss.

[2] Spin tracking in Zgoubi dates back to the early 1990s, and has been subject to extensive benchmarking, including long-term tracking in rings [23], and spin diffusion as in the present exercise.

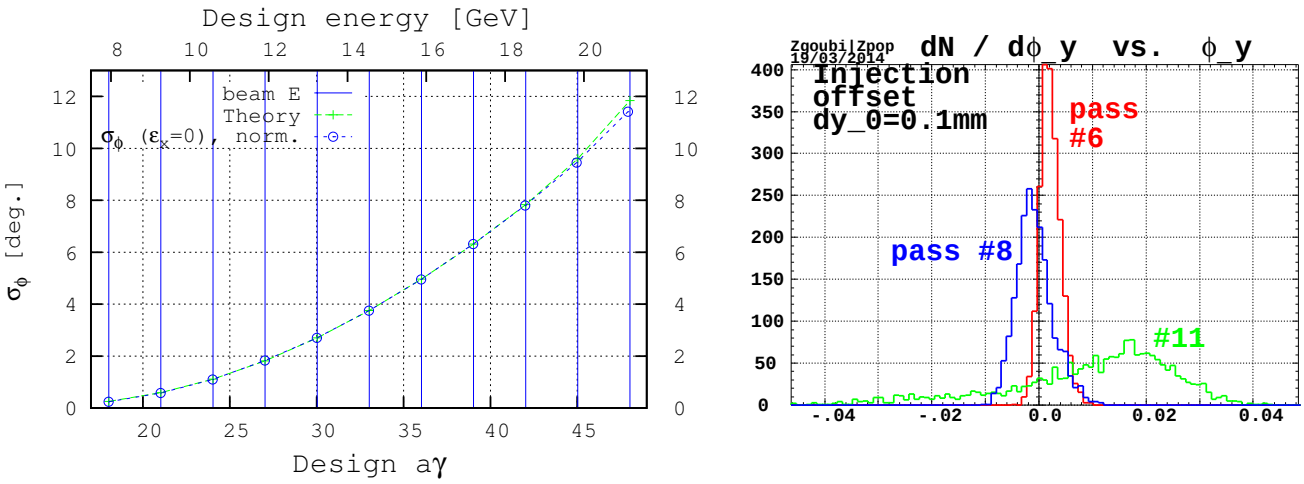

Figure 24: Polarization loss. Left : from energy spread, including theoretical expectation [24]. Right : vertical spin angle spread, in the presence of initial vertical beam jitter.

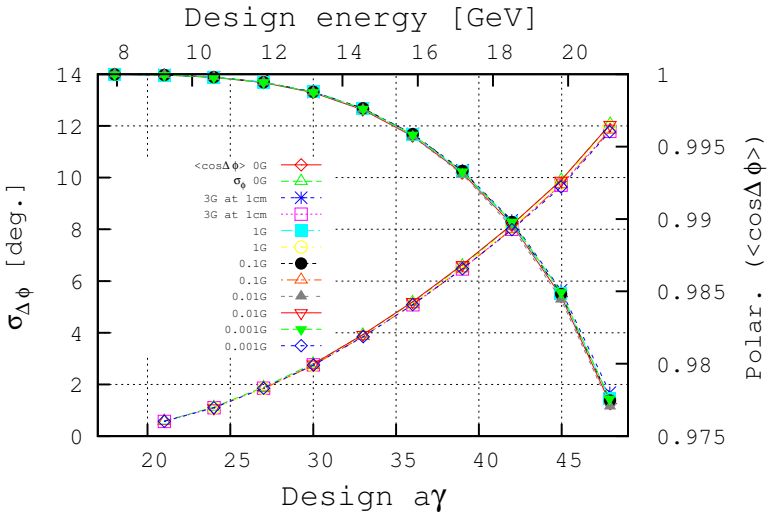

Figure 25: Polarization (right vertical axis) and spin angle spread (left axis) in the presence of dodecapole errors.

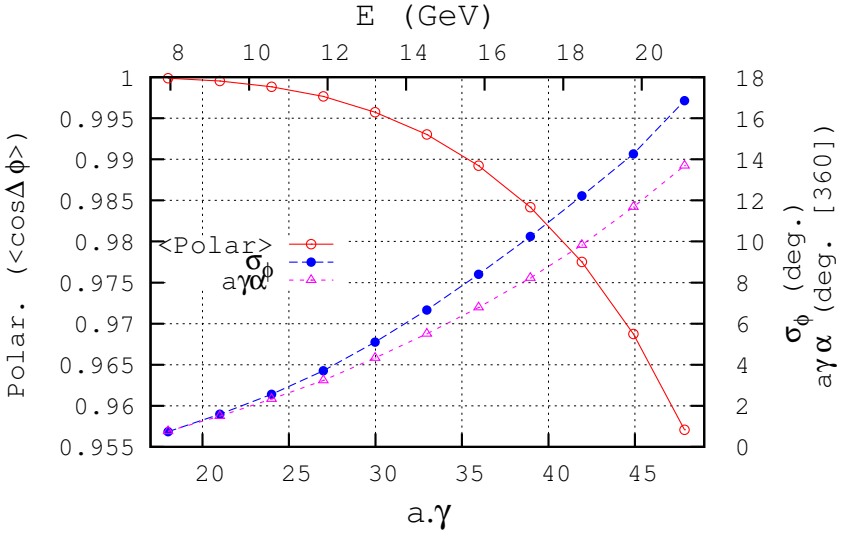

Figure 26: Polarization, spin angle spreading, precession, in the conditions of Figs. 21, 22.

6 Multiple-beam orbit correction

A first approach to multiple-beam orbit correction uses a matching procedure, in which the theoretical FFAG orbit is imposed on the bunch centroid in the arcs, for each energy. The constraint is imposed every 23 cells, this makes 6 such sections to be corrected in a 138 cell arc. That allows 23 variables (H-correctors at all quadrupoles) for 22 constraints (x and x' for each one of the 11 energies, in one go). A 50 particle bunch is considered for the matching.

As an illustration, a strong horizontal orbit defect is injected in the arc quadrupoles, namely, a vertical dipole error $b_0 \in [-20, +20]$Gauss (equivalent to misalignment $\Delta x = \pm 40\,\mu$m), random uniform. As a consequence the *rms* concentration ellipse surface in the absence of correction would be far beyond even what the earlier Fig. 21 shows. Fig. 27 displays the evolution of the horizontal *rms* concentration ellipse surface after applying that orbit correction scheme in the arcs (orbit correction uses dipole correctors located in drifts between quadrupoles), given initial conditions, at 7.944 GeV, $\epsilon_x \approx \epsilon_y \approx 50\,\pi\mu$m and $dE/E = 0$. This result is promising (the surge at $a\gamma \approx 27$ is again an *apparent rms* concentration ellipse surface increase resulting from a surge in bunch off-centering at that particular pass/energy in the eRHIC ring).

An option in this method is to apply the constraint cell after cell, in a running mode all around the ring (in both planes in addition, in the presence of both horizontal and vertical multipole defects), until the residual orbit causes tolerable residual emittance growth.

A different type of constraint, rather than the theoretical FFAG orbits, is to request minimal bunch oscillation amplitude in the cells, leaving the average orbit free. This would have the merit of allowing a self-adjustment of the FFAG orbit on the actual bunch centroid energy (which is not the design one, due to SR for instance). This is an on-going study.

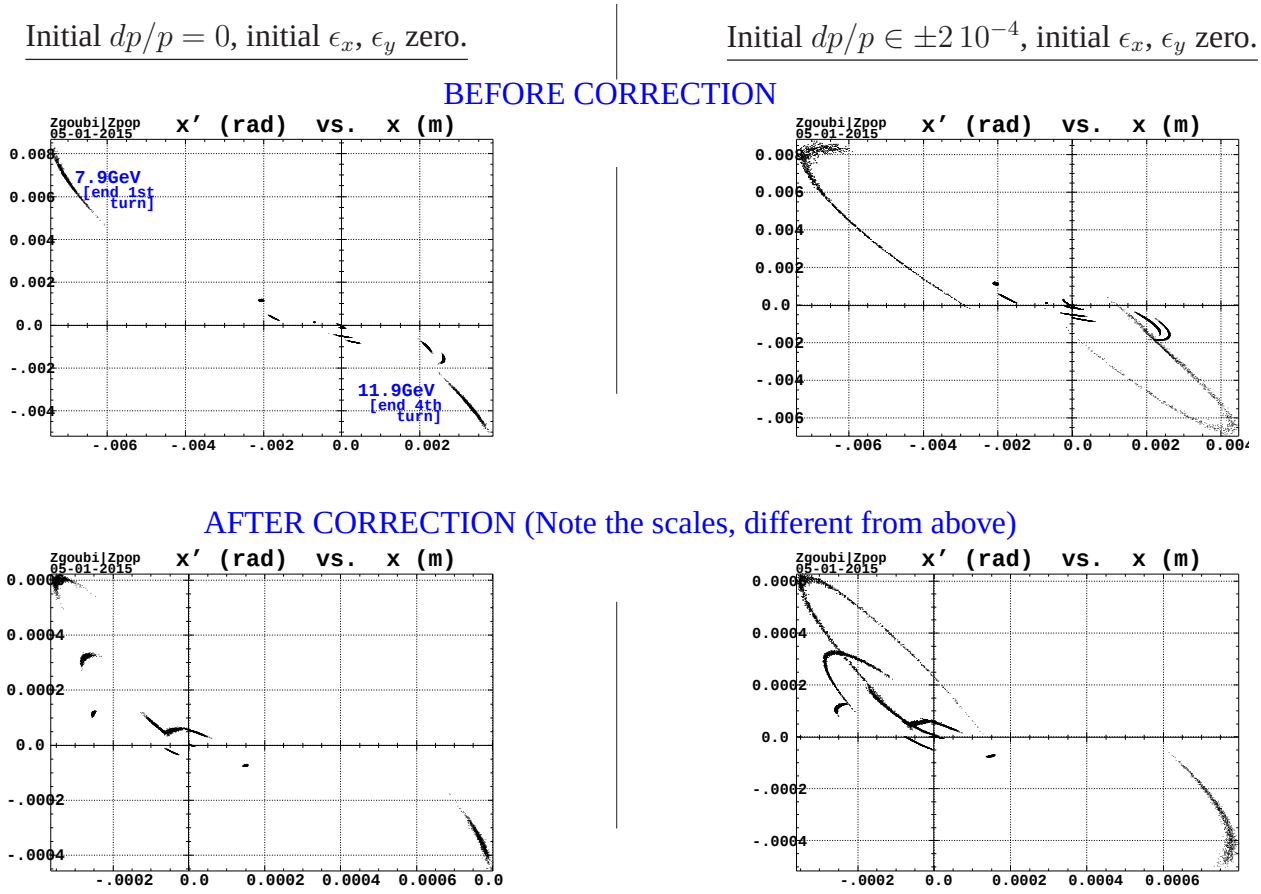

Figure 27: Single-turn phase space portraits (5000 particles in a bunch), in the presence of a $b_0 \in [-20, +20]$Gauss random uniform dipole field defect, either before correction (top row) or after correction (bottom row). Transverse emittances at start of the turn are taken null, initial momentum spread is either zero (left column) or random uniform in $[-2 \times 10^{-4}, +2 \times 10^{-4}]$ (right column).

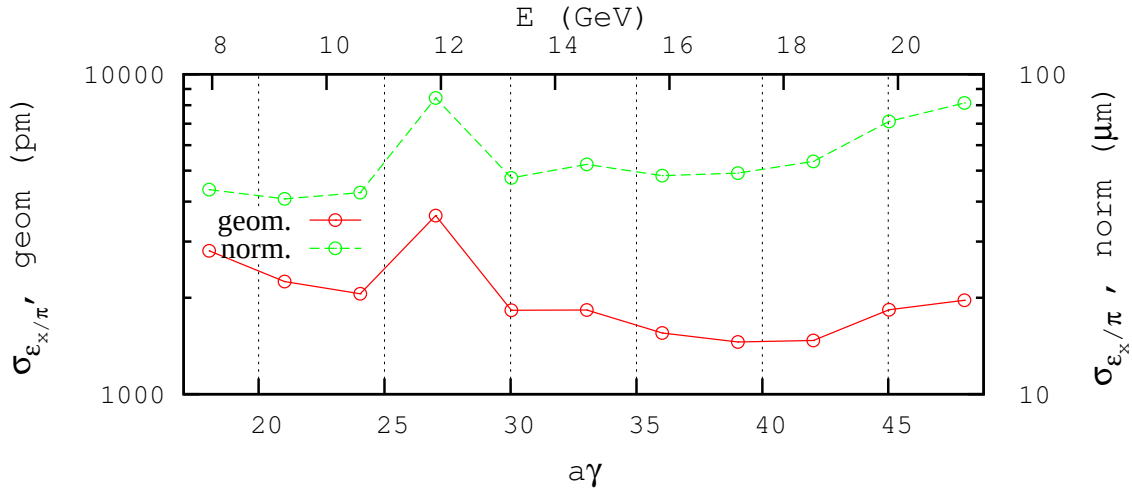

Figure 28: Evolution of the single-turn *rms* concentration ellipse surface growth (the line is to guide the eye), in the presence of a *corrected* $b_0 \in [-20, +20]$Gauss random defect.

APPENDIX

A Field in the FFAG quadrupoles

The scalar potential from which are derived the $2n$-pole multipole field and derivatives $\frac{\partial^{i+j+k}\vec{B}_n(X,Y,Z)}{\partial X^i \partial Y^i \partial Z^k}$ ($i+j+k=0$ to 4) as needed in the ray-tracing method is [29]

$$V_n(X,Y,Z) = (n!)^2 \left(\sum_{q=0}^{\infty} (-1)^q \frac{G^{(2q)}(X)(Y^2+Z^2)^q}{4^q q!(n+q)!} \right) \left(\sum_{m=0}^{n} \frac{\sin\left(m\frac{\pi}{2}\right) Y^{n-m} Z^m}{m!(n-m)!} \right) \tag{4}$$

where $G(X)$ is a longitudinal form factor, defined at the entrance or exit of the optical element by

$$G(s) = \frac{G_0}{1+\exp(P(s))}, \quad G_0 = \frac{B_0}{R_0^{n-1}} \tag{5}$$

wherein B_0 is the field at pole tip radius R_0, and

$$P(s) = C_0 + C_1\left(\frac{s}{\lambda}\right) + C_2\left(\frac{s}{\lambda}\right)^2 + C_3\left(\frac{s}{\lambda}\right)^3 + C_4\left(\frac{s}{\lambda}\right)^4 + C_5\left(\frac{s}{\lambda}\right)^5$$

and s is the distance to the EFB.

This model yielded the field shown in Fig. 3 and Fig. 29.

B Cell simulation with fringe fields

The fringe field simulation shown in Fig. 29 is that used in DA estimates, Fig. 15.

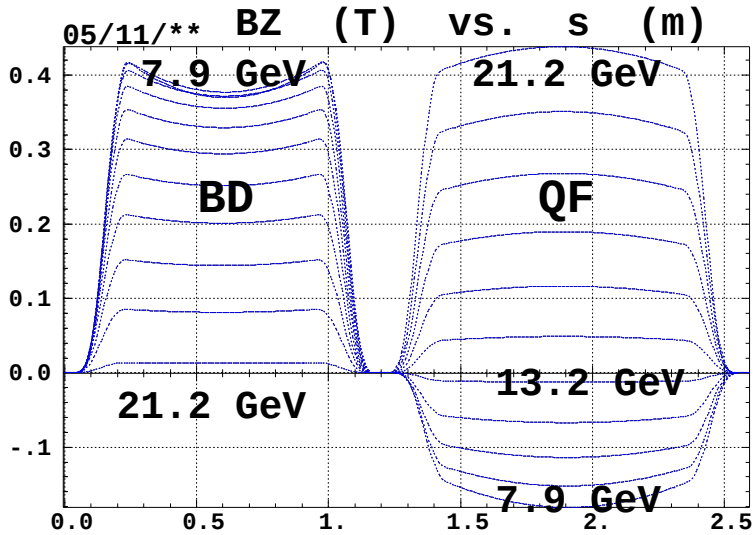

Figure 29: Magnetic field along the 11 orbits across the FFAG cell, in the soft-edge model, in the BD (left) and QF (right) magnets.

The corresponding Zgoubi cell data list is as follows :

```
'DRIFT'    DRIF      HD
14.38218115
'MULTIPOL' MULT      BD2
2  .Mult
90.805000 10.00    0.0000000000   -0.8631366333 0.0 0.0 0.0 0.0 0.0 0.0 0.0 0.0
10  8. 1.00 0.0 .0 0.0 .0 0.0 .0 0.0 .0
6 -.010967  5.464823  .996848 1.568787 -5.671630 18.505734                      BD2
10  8. 1.00 0.0 .0 0.0 .0 0.0 .0 0.0 .0
6 -.010967  5.464823  .996848 1.568787 -5.671630 18.505734                      BD2
#30|91|30   Mult  BD2
3 0.    3.90109800E-01  -1.52878350E-03
'DRIFT'    DRIF      D
28.76436230
'MULTIPOL' MULT      QF2
0  .Mult
109.855000 10.00    0.0000000000    0.8631366333 0.0 0.0 0.0 0.0 0.0 0.0 0.0 0.0
10  8. 1.00 0.0 .0 0.0 .0 0.0 .0 0.0 .0
6 -.010967  5.464823  .996848 1.568787 -5.671630 18.505734                      QF2
10  8. 1.00 0.0 .0 0.0 .0 0.0 .0 0.0 .0
6 -.010967  5.464823  .996848 1.568787 -5.671630 18.505734                      QF2
0. 0. 0. 0. 0. 0. 0. 0. 0. 0.
#30|110|30   Mult  QF2
3 0.   -3.90109800E-01  -1.84950850E-03
'DRIFT'    DRIF      HD
14.38218115
```

References

[1] D. Trbojevic, FFAG Lattice Design of eRHIC and LHeC, EIC'14 workshop, http://appora.fnal.gov/pls/eic14/agenda.full ;

[2] E.C. Aschenauer et als., "eRHIC Design Study, Electron-Ion Collider at BNL", arXiv:1409.1633, Sept. 2014.

[3] M. Blaskiewicz, Electron Acceleration for eRHIC in FFAG, FFAG 2006 workshop, BNL (http://www.cap.bnl.gov/ffag-2006/presentations/talks.htm).

[4] Shane Koscielniak, Thin-Element and Thick-Element Optimizations of Non-Scaling FFAG Lattices, FFAG 2004 Workshop, April 15-21, TRIUMF.

[5] Shane Koscielniak, Doublet, F0D0, Tripet, lattices for muon and electron FFAGs - low & high B-field, low & high volts/cell, FFAG 2004 Workshop, April 15-21, TRIUMF.

[6] M.K. Craddock, An analytical approach to FFAG optics, FFAG 2004 Workshop, April 15-21, TRIUMF.

[7] M.K. Craddock and S.R. Koscielniak, Orbit properties of non-scaling FFAG accelerators using constant-gradient magnets, Procs. PAC'07 Conf., Albuquerque, June 25-29.

[8] F. Méot, The ray-tracing code Zgoubi - Status, NIM A 767 (2014) 112125

[9] M.K. Craddock, FFAG Tracking Studies using CYCLOPS, (https://indico.fnal.gov/conferenceOtherViews.py?view=standard&confId=2672).

[10] F. Méot, Status of Computer Codes, FFAG 2006 workshop, BNL (http://www.cap.bnl.gov/ffag-2006/presentations/talks.htm).

[11] J. Scott Berg, Correct Tracking in FFAGs, FFAG'05 workshop, 5-9 December 2005, Kyoto University.

[12] E.D. Courant et al., A comparison of several lattice tools for computation of orbit functions of an accelerator, Procs PAC'03 Conf., May 12-16.

[13] F. Méot, 6-D beam dynamics simulations in FFAGs using the ray-tracing code Zgoubi, ICFA Beam Dyn.Newslett.43:44-50 (2007).

[14] D. Trbojevic, S. Brooks, http://www.cadops.bnl.gov/eRHIC/erhicWiki/images/2/2b/Meeting_030514_3.pdf

[15] N. Tsoupas et al., The Optics of the Low Energy FFAG cell of the eRHIC collider, using realistic field maps, Tech. Note C-A/eRHIC/1 (2015).

[16] D. Poirier, Etude des défauts de champ magnétiques de MIMAS et correction de la chromaticité de Super-ACO, PhD Thesis, Orsay, 1984.

[17] F. Méot, Simulation of radiation damping in rings, using stepwise ray-tracing methods, 2015 JINST 10 T06006 (June 2015).

[18] F. Méot et al., End-to-end 9-D polarized bunch transport in eRHIC [...], IPAC15 Conf. Procs. (Richmond, 2015).

[19] F. Méot, End-to-end, 9-D, Polarized Radiative Bunch Dynamics Simulations in eRHIC ERL, EIC'14 workshop, http://appora.fnal.gov/pls/eic14/agenda.full ; F. Méot, Beam and Polarization Dynamics in Electron FFAG Lattices, ERL 2015 workshop, https://indico.bnl.gov/conferenceDisplay.py?confId=909.

[20] G. Leleux et al., Synchrotron radiation perturbation in transport lines, Part. Acc. Conf., San Francisco, May 6-9, 1991.

[21] https://oraweb.cern.ch/pls/hhh/code_website.disp_code?code_name=BETA

[22] F. Méot, J. Payet, Simulation of SR loss in high energy transport lines, Rep. CEA DSM DAPNIA/SEA-00-01 (2000).

[23] F. Méot, A numerical method for combined spin tracking and ray tracing of charged particles, NIM A 313 (1992) 492-500;
F. Méot et al., Spin tracking simulations in AGS based on ray-tracing methods, Tech. Note C-A/AP/452 (2010).

[24] V. Ptitsyn, Electron Polarization Dynamics in eRHIC, EIC 14 workshop, JLab, 17-21/03/2014.

[25] D. Trbojevic, FFAG Lattice Design of eRHIC and LHeC, EIC 2014 workshop, Newport News (17-21 March 2014).

[26] D. Trbojevic et al., ERL with non-scaling fixed field alternating gradient lattice for eRHIC, IPAC15 Conf. Procs. (Richmond, 2015).

[27] D. Trbojevic, private communication.

[28] V. Ptitsyn, Electron Polarization Dynamics in eRHIC, EIC'14 workshop, http://appora.fnal.gov/pls/eic14/agenda.full.

[29] F. Méot, Zgoubi users' guide, http://www.osti.gov/scitech/biblio/1062013